Blood-based biomemristor for hyperglycemia and hyperlipidemia monitoring

Kaikai Gao [a,b,c,d], Bai Sun [a,b,c,d,*], Guangdong Zhou [e], Zelin Cao [a,b,c,d], Linbiao Xiang [a,b], Jiawei Yu [a,b], Ruixin Wang [a,b], Yingmin Yao [a,b], Fulai Lin [a,b], Zhuoqun Li [a,b], Fenggang Ren [a,b], Yi Lv [a,b], Qiang Lu [a,b,**]

[a] *Department of Geriatric Surgery, The First Affiliated Hospital of Xi'an Jiaotong University, Xi'an, Shaanxi, 710061, China*
[b] *National Local Joint Engineering Research Center for Precision Surgery and Regenerative Medicine, The First Affiliated Hospital of Xi'an Jiaotong University, Xi'an, Shaanxi, 710061, China*
[c] *Frontier Institute of Science and Technology (FIST), Xi'an Jiaotong University, Xi'an, Shaanxi, 710049, China*
[d] *Micro-and Nano-technology Research Center, State Key Laboratory for Manufacturing Systems Engineering, Xi'an Jiaotong University, Xi'an, Shaanxi, 710049, China*
[e] *College of Artificial Intelligence, Brain-inspired Computing & Intelligent Control of Chongqing Key Lab, Southwest University, Chongqing, 400715, China*

ARTICLE INFO

ABSTRACT

Thanks to its structural characteristics and signal patterns similar to those of human brain synapses, memristors are widely believed to be applicable for neuromorphic computing. However, to our knowledge, memristors have not been effectively applied in the biomedical field, especially in disease diagnosis and health monitoring. In this work, a blood-based biomemristor was prepared for in vitro detection of hyperglycemia and hyperlipidemia. It was found that the device exhibits excellent resistance switching (RS) behavior at lower voltage biases. Through mechanism analysis, it has been confirmed that the RS behavior is driven by Ohmic conduction and ion rearrangement. Furthermore, the hyperglycemia and hyperlipidemia detection devices were constructed for the first time based on memristor logic circuits, and circuit simulations were conducted. These results confirm the feasibility of blood-based biomemristors in detecting hyperglycemia and hyperlipidemia, providing new prospects for the important application of memristors in the biomedical field.

1. Introduction

With the explosive expansion and evolution of the food industry, diets and beverages catering to people are becoming increasingly diverse. Against the backdrop of a fast-paced lifestyle, unhealthy eating habits, excessive intake of sugary beverages, and lack of physical activity have contributed to a surge in the number of individuals with hyperglycemia (HGY) and hyperlipidemia (HLP) [1–4]. Persistent HGY and HLP are associated with an increased risk of cardiovascular diseases, visual impairment, and organ disorders [5,6]. Therefore, regular blood glucose and lipids monitoring is essential for overall health and chronic disease prevention. Nowadays, the blood glucose meters are a commonly used self-monitoring device, allowing for real-time monitoring of blood glucose without the intervention of healthcare personnel [7–9]. However, the detection of HLP still primarily relies on clinical lipoprotein electrophoresis, and real-time monitoring of blood lipids in vitro remains a significant challenge.

It is widely acknowledged that numerous electronic devices have been specifically designed for clinical detection, playing a pivotal role in advancing medical diagnostics. Consequently, an increasing number of researchers are continuously engaged in the design, enhancement, and optimization of electronic components to make them more suitable for medical applications. Gao et al. fabricated a wearable biosensor on PET capable of selectively detecting sodium and potassium ions in sweat. This innovative device enables real-time detection and provides feedback in the form of electrical signals [10]. Their study stands out as a landmark paper in the field of medical non-invasive detection devices. In a notable contribution, Boutry et al. presented an implantable piezoelectric transducer crafted entirely from biodegradable materials, which exhibits remarkable sensitivity, responding to pressures as low as 12 Pa. Its excellent biocompatibility positions it as a key player in various finely tuned medical treatments [11]. Additionally, Xu et al. developed an

---

exceptionally small hydrophilic nanoreactor on TiO₂ nanotube arrays. This device demonstrated high selectivity and sensitivity to proteins, achieving impressive response values ranging from 2 U/L to 200 U/L for alkaline phosphatase concentrations [12]. In the same year, Su et al. introduced a paper-based biosensor integrated with Raman spectroscopy. This integration enables precise diagnosis of breast cancer and the differentiation of various exocytosis proteins in the serum of breast cancer patients. Such advancements significantly enrich personalized detection protocols for breast cancer today [13]. Beyond the aforementioned devices, various resistors, capacitors, and transistors have been developed for medical monitoring. Concurrently, the spectrum of tested organisms is diversifying, encompassing blood, tissues, metabolites, and hair [14–18].

As the fourth fundamental electronic component, following resistors, capacitors, and inductors, the memristor stands out as a nonlinear resistor with charge memory capabilities [19]. This device boasts a compact physical size, extremely low power consumption, and compatibility with CMOS processes [20,21]. For a long time, its application scope has centered around information storage, logic operations, and analog neural networks [22–26]. In recent years, the design of memristors for use in the field of life medicine has attracted much attention [27,28]. For example, Yan et al. reported a flexible egg protein-based memristor for simulating neuromimetic behaviours, including short-term plasticity and long-term plasticity [29]. Desai et al. attempted to fabricate a memristor via trypsin hydrogel, and the device also successfully simulated the typical neural behaviour of spike-time-dependent plasticity [30]. However, to our knowledge, there are currently no reports on memristors used for disease monitoring.

The unique sandwich-like structure of the memristor, where the interstitial dielectric layer material plays a crucial role in determining the electrical characteristics of the device, raises the question of whether rapid response under various medical detection targets can be achieved by utilizing the body fluids of an organism as the dielectric layer material. Exploring the feasibility of this concept is crucial for broadening the application domains of memristors and realizing medical in vitro detection, particularly for real-time detection of HLP. In this study, we fabricated a biomemristor using blood from healthy rats as the sole dielectric layer material. The device

demonstrates an excellent RS window at lower voltage biases (±1 V). The RS behavior of the device is driven by Ohmic conduction and ionic rearrangement, as indicated by further fitting the *I–V* curve and modeling of charge transport. Subsequently, we modeled rats suffering from HGY and HLP and fabricated memristors using their blood, which exhibited different electrical properties compared to healthy blood. Finally, it was firstly developed a device for rapid in vitro detection of HGY and HLP based on the memristor logic circuit and successfully conducted circuit simulations. The output of the circuit simulation demonstrates significant differentiation between HGY/HLP and healthy blood.

These results are exciting and expand the application of memristors in life sciences. This study underscores the compatibility of memristors with logic circuits and highlights their potential in medical monitoring. Notably, it provides a personalized in vitro solution for HLP detection with significant commercial viability. Furthermore, this work inspires further exploration of the memristor-based smart medical solutions.

2. Results and discussion

A typical memristor with an Ag/Blood/Ti/Glass structure is reported. The major fabrication process is illustrated in Fig. 1a. Initially, blood was collected from the jugular vein of a healthy rat and subsequently spin-coated onto Ti/Glass substrates. Following the natural coagulation of the blood, Ag electrodes were sputtered onto the blood film layer using magnetron sputtering, completing the fabrication of the device. During electrical characterization tests, a voltage bias sequence was applied to the top electrode (Ag), while the bottom electrode (Ti) remained grounded [31]. A photograph of the fabricated device and a model of the double-ended structure are provided (Fig. S1). Fig. 1b presents the cross-sectional morphology of the device, whereby it can be shown that the film thickness of the blood dielectric layer is about 2 μm and the thickness of the Ti electrode is about 200 nm. To analyze the chemical composition and distribution of the blood dielectric layer, EDS (Fig. 1c–g) and FT-IR (Fig. S2) tests were performed. The EDS mapping indicates the predominant presence of elements such as Na, Mg, K, and Ca in the dielectric layer, with the inset providing a planar area scanned for the dielectric layer (scale 10 μm). In addition, the FT-IR spectra show
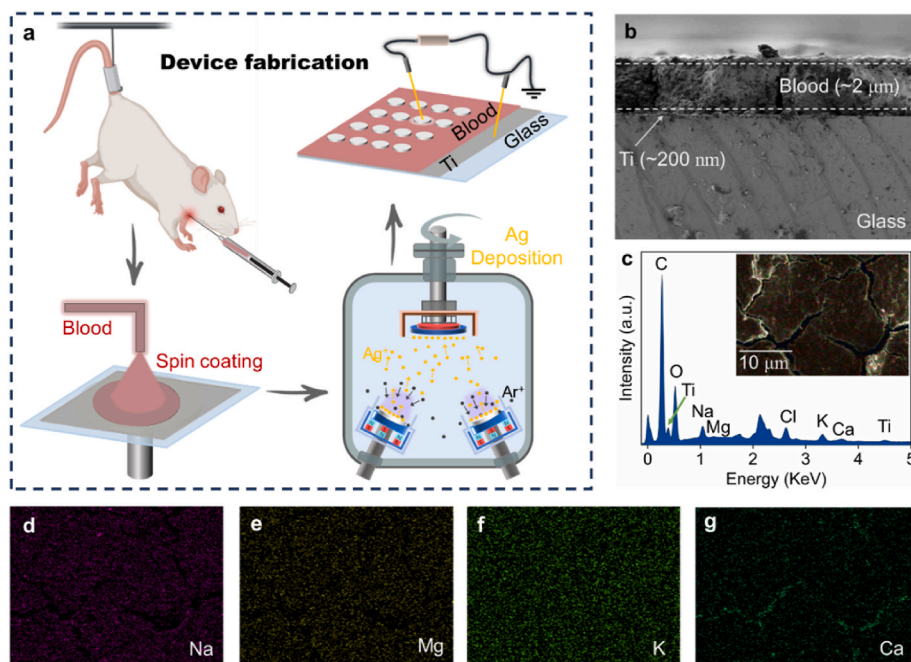

Fig. 1. Device fabrication and structural characterization. (a) Flowchart for the fabrication of the memristor with an Ag/Blood/Ti/Glass structure. (b) Device cross-section structure. (c) Device plane EDS analysis. The inset image shows the scanned area. (d–g) Distribution of different elements under the EDS test.

strong absorption peaks near 3306 cm^{-1} (corresponding to C–H stretching vibration), 1653-1542 cm^{-1} (corresponding to C=C stretching vibration) and 621 cm^{-1} (corresponding to C–H bending vibration), which corresponds to various types of biomolecules in the cell, including sugars, lipids and proteins [32,33]. Thus, the dielectric layer is identified as a blood film, with no other impurities observed.

In the initial phase, the biomemristor with an Ag/Blood/ITO structure was fabricated by directly spin-coating fresh blood from healthy rats onto ITO substrates. The fabrication process and electrical characterization of the device are illustrated in Fig. S3. Surprisingly, during electrical characterization, the device exhibited extremely stable RS behavior and endured up to 500 cycles. While this result is encouraging, concerns arose regarding the potential impact of the indium tin oxide coating on the commercially available ITO substrate on the test results [34,35]. Consequently, the substrate was changed to Ti/Glass while maintaining a consistent device fabrication process. Fig. 2a illustrates the electrical characteristics of the Ag/Blood/Ti/Glass-structure memristor, with the sequence of voltage biases (0 V → 1 V → −1 V → 0 V) applied to the device shown in the inset. This device continues to exhibit excellent RS behavior at lower voltage biases. Subsequently, the *I–V* characteristic curves on a semi-logarithmic scale are plotted as depicted in Fig. 2b, indicating the volatile RS properties of the fabricated devices. To explore the repeatability of RS, the corresponding low and high resistance states (LRS and HRS) at a voltage bias of 0.5 V were extracted (Fig. 2c). As the number of cycles increases, the LRS remains in a steady state, while the HRS, despite experiencing some fluctuations, remains distinguishable from the LRS, with an HRS/LRS ratio of 10^1. The stability and reliability of RS characteristics are maintained. Furthermore, the distributions of HRS and LRS of the devices are tabulated in Fig. 2d, with the curves representing Gaussian fitting results. It can be concluded that the LRS of the device is predominantly concentrated at 235 Ω, while the HRS is primarily concentrated at 2350 Ω. This outcome is desirable, as the higher discrimination between the LRS and HRS suggests lower misreading rate for this device in practical storage and computing applications [31,36].

To comprehensively investigate the impact of different voltage biases on the electrical characteristics of the device, various voltage bias sequences were applied to the top electrode (Ag). When the sequence 0 V → 0.5 V → −0.5 V → 0 V was applied, the device failed to exhibit RS behavior (Fig. S4). This failure could be attributed to the insufficient lower voltage bias, which did not provide the necessary potential energy for ion migration in the dielectric layer. Consequently, the various ions in the blood dielectric layer maintained their initial distribution, failing to induce a significant change in the resistance value. Conversely, when a larger voltage bias sequence (0 V → 1.5 V → −1.5 V → 0 V) was applied to Ag, the RS window of the device in the negative voltage region decreased compared to that observed in Fig. 2a, while the positive voltage region continued to exhibit better RS behavior (Fig. 2e). The *I–V* characteristic curves presented in Fig. 2f under a semi-logarithmic scale also support this observation. This asymmetry could potentially be attributed to the enhanced ionization process of Ag under high voltage bias and its continued incorporation into the dielectric layer, resulting in a change in the resistive state of the device [37]. Notably, considering blood as an unconventional memristor dielectric material, elucidating its RS mechanism is imperative, which will be the focus of the subsequent discussion.

Fig. 3a shows the *I–V* characteristic curves for the 1st and 50th turns of the Ag/Blood/Ti/Glass-structure memristor under a fixed voltage bias sequence (0 V → 1 V → −1 V → 0 V), with the arrows indicating the order of charge flow. Initially, the device is maintained at LRS, and as the voltage is incremented from 0 to 1 V, an abrupt decrease in the current value occurs near 1 V, corresponding to the switching of the device to HRS and RESET. Subsequently, the device switches from HRS formation to LRS near −0.5 to −1 V, corresponding to the SET process. The alternation of the RESET and SET processes repeatedly gives the device its typical switching characteristics [38]. Further insights into the principles governing LRS and HRS switching are attained through additional fitting of *I–V* characteristic curves and modeling of charge transport. The log|I| - log|V| curves of the fabricated devices in the positive voltage region are depicted in Fig. 3b. The slopes of the curve fit
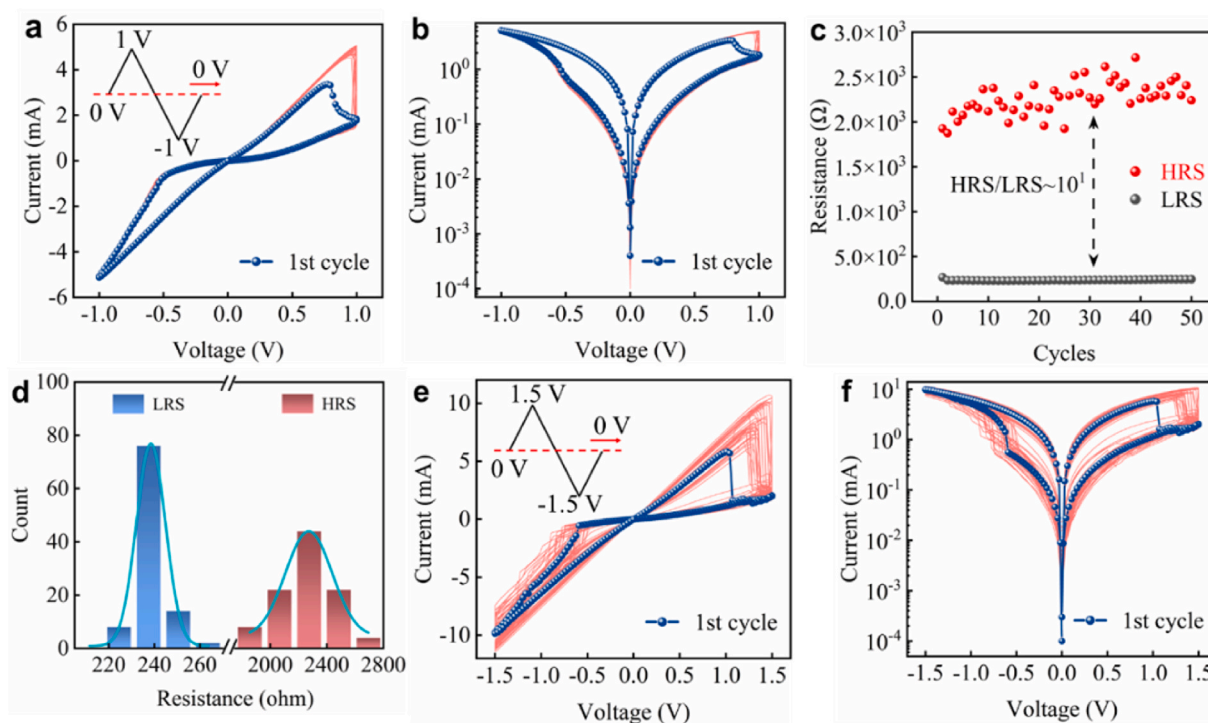
Fig. 2. Electrical characteristics of memristor with an Ag/Blood/Ti/Glass structure. (a) A typical *I–V* curve of the device. The inset shows the voltage bias parameters applied to the device: 0 V → 1 V → −1 V → 0 V. (b) *I–V* curve in the semi-log scale. (c) Endurance test of the resistance switching for 50 cycles. (d) Frequency distribution of LRS and HRS. (e–f) Electrical characteristics of the device at 0 V → 1.5 V → −1.5 V → 0 V voltage bias.
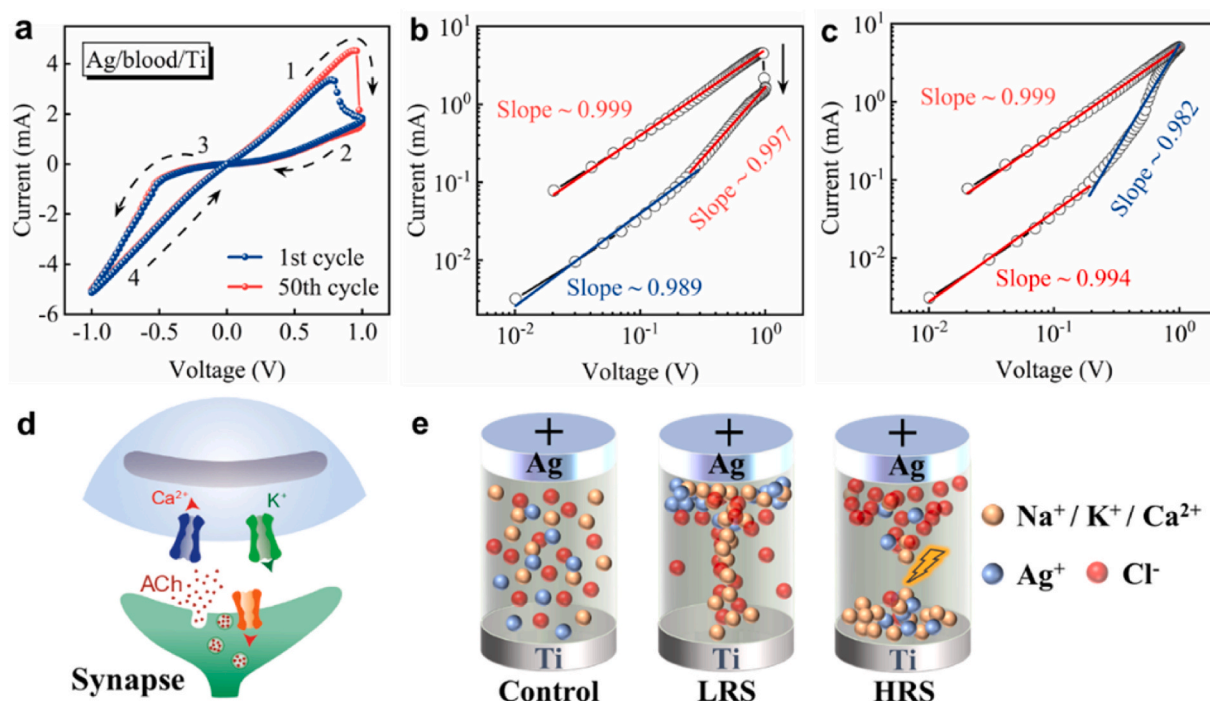
Fig. 3. Resistance switching mechanism of the blood memristor with an Ag/Blood/Ti/Glass structure. (a) The typical *I–V* curve of the device at the first and 50th revolutions. (b) Fitting results for stages 1 and 2 in Fig. 4a. (c) Fitting results for stages 3 and 4 in Fig. 4a. (d) Brief sketch of the signal conduction between neurons. (e) Formation and breakage of conductive filament during LRS and HRS switching.

are 0.999 and 0.997 for the two phases where the voltage increases from 0 to 1 V and decreases from 1 to 0 V, respectively, closely approximating 1. These findings indicate that the charge transfer behavior of the device in the positive voltage bias region predominantly adheres to ohmic conduction [39,40], corresponding to equations (1) and (2).

$$I_{Ohmic} = q\mu N_C V \exp\left(\frac{-(E_c - E_f)}{kT}\right) \tag{1}$$

$$I \propto V \exp\left(\frac{-\Delta E_x}{kT}\right) \tag{2}$$

where μ and Nc represent the electron mobility and conduction band effective density, respectively. ΔE_x (E_c-E_f) is the activation energy of electrons. Simply put if the charge transfer process satisfies I ∝ V (slop ~ 1), it is attributable to ohmic conduction. Interestingly, when we further fit the log|I| - log|V| curve in the negative voltage region of the device, the fitting results still satisfy the ohmic conduction (Fig. 3c). It can be seen that the electrical properties of memristors fabricated based on blood are mainly driven by ohmic conduction.

Memristors exhibit signaling akin to synaptic connections between neurons in the human brain [41,42]. From a synaptic perspective (Fig. 3d), multiple neurons act as a bridge for signal transmission during the process of stimulus generation and recognition by the human brain [43]. Initially, the preceding neuron receives the stimulus, generating an action potential that triggers the release of neurotransmitters into the synaptic gap. Subsequently, appropriately shaped and structured neurotransmitters are received by the nest neuron, which in turn transmits the stimulus [44]. Viewing the phenomenon from the perspective of the blood memory blocker (Fig. 3e), the presence of a large number of Na⁺, K⁺, Ca²⁺, Cl⁻, etc., in the blood keeps the initial state of the top and bottom electrodes connected, allowing the device to exhibit LRS. After applying a positive voltage bias, the Ag at the top electrode is oxidized and releases Ag⁺ into the dielectric layer, and then moves to the bottom electrode and is reduced to Ag. The continuous buildup of Ag breaks the initial ionic arrangement in the dielectric layer, causing the on-state to

be interrupted, and the device switches to the HRS. When the voltage bias is reversed, the stacked Ag undergoes oxidation to Ag⁺ followed by its reduction to Ag at the top electrode. This process restores the ionic arrangement in the blood to its initial state, causing the device to transition back to the LRS. The redox equations involved in the top electrode Ag throughout the voltage bias sequence are shown in Eqs (3) and (4), respectively [45].

$$Ag \rightarrow Ag + e^- \tag{3}$$

$$Ag^+ + e^- \rightarrow Ag \tag{4}$$

The top electrode Ag is first oxidized to Ag⁺ and then moves to the bottom electrode driven by the electric field force to be reduced to Ag.

The relative levels of various biomolecules in the blood can serve as indicators of the organism's health status [46]. In the medical field, analyzing the concentration of each component in collected blood can help determine the presence of diseases [47]. Additionally, the electrical characteristics of a memristor are primarily influenced by the composition of the dielectric layer [48]. Motivated by these observations, we endeavored to collect fresh blood from rats with conditions such as HGY and HLP to fabricate memristors. We aimed to investigate whether the devices fabricated from such blood samples would exhibit electrical characteristics distinct from those of memristors fabricated using healthy blood. These rats were procured from the Affiliated Hospital of Xi'an Jiaotong University. Fig. 4a depicts the process of establishing the HGY and HLP rat models, with specific methodologies detailed in the experimental section of this study. Here, the memristor fabricated from healthy rat blood was used as a control (labeled control-memristor). The *I–V* characterization curves of Control-, HGY-, and HLP-memristors are shown in Fig. 4b. Unlike the RS behavior observed in the control-memristor, the HGY- and HLP-memristor did not exhibit a significant RS window. The possible reason for this is that the excessive blood glucose and lipid concentrations in the blood severely interfered with the ionic rearrangement during the charge transfer process in the device. Under the same voltage bias (0 V → 1.5 V → −1.5 V → 0 V), the main difference between the *I–V* characteristic curves of the
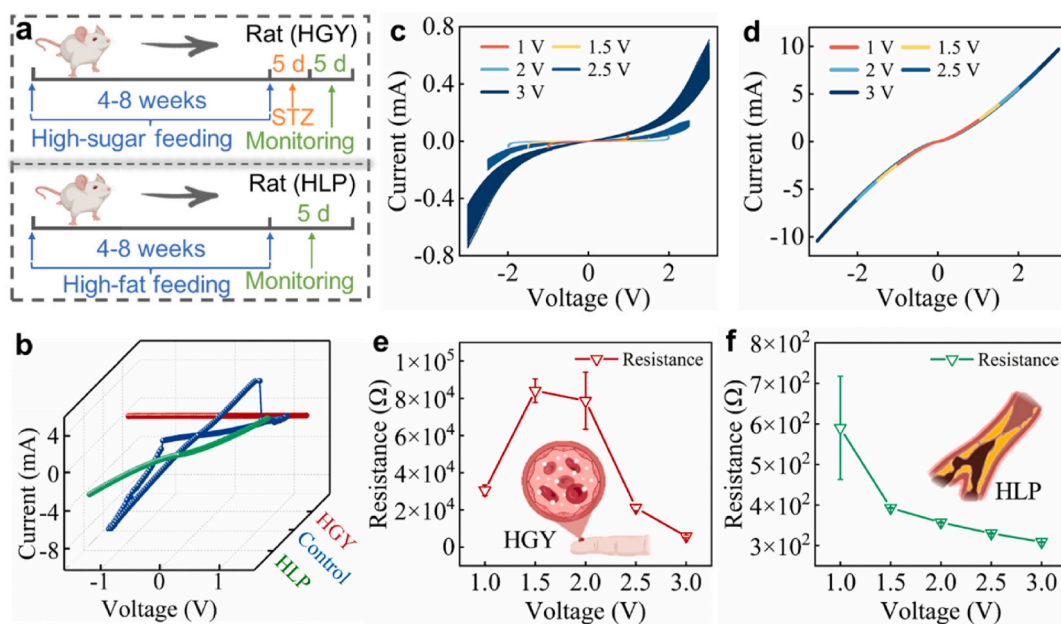
Fig. 4. Electrical characterization of HGY-, HLP-memristors. (a) Modeling of HGY and HLP rats. (b) *I–V* characterization curves based on control-, HGY- and HLP-memristors, which correspond to blue, red and green, respectively. (c, d) Effect of different voltage biases on the electrical characteristics of HGY- and HLP-memristor. (e, f) Device resistance value response to peak voltage.

HGY-memristor and the HLP-memristor lies in their peak currents, which reach approximately 0.02 mA and 3.83 mA, respectively (Fig. 4b).

To further investigate the effects of different voltage biases on the

electrical characteristics of HGY- and HLP-memristors, we applied voltage biases of ±1, ±1.5, ±2, ±2.5, and ±3 V to the top electrode of the device, as illustrated in Fig. 4c and d, respectively. The results indicate that the current output of the HGY-memristor fluctuates greatly
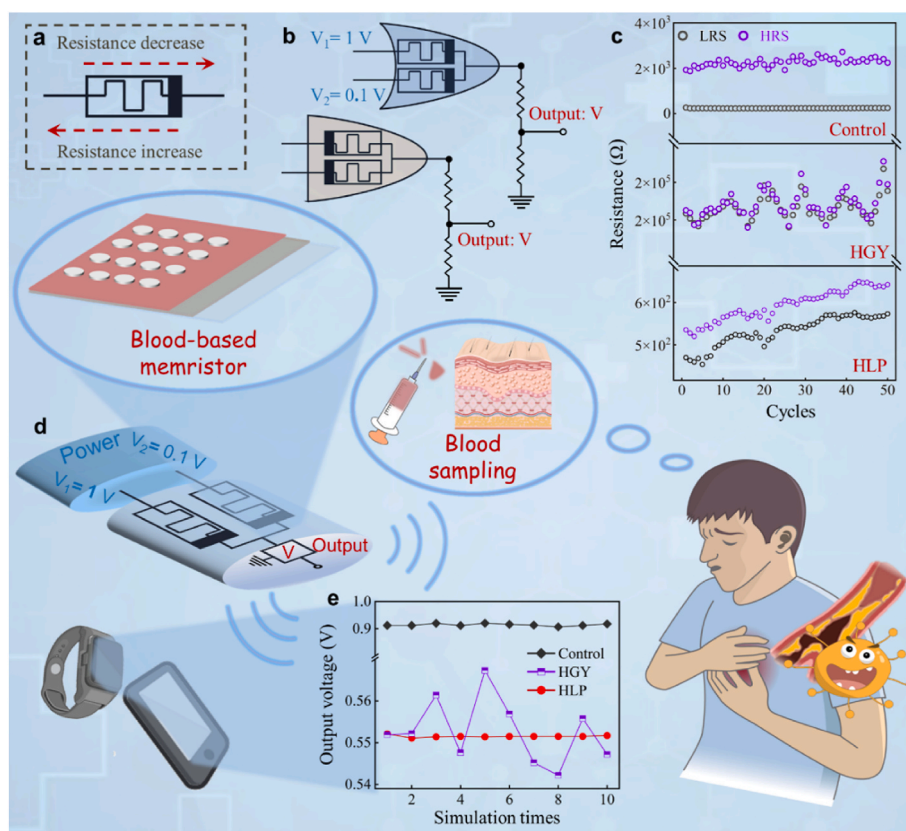
Fig. 5. A flexible in vitro HGY and HLP monitoring device. (a) Schematic diagram of the equivalent circuit of a memristor. (b) Circuit diagrams of monitoring device. (c) Endurance test of the control-, HGY- and HLP-blood memristors. (d) Structure schematic diagram of the monitoring device. (e) Circuit simulation results for HGY and HLP models.

with increasing applied voltage bias, whereas the current output of the HLP-memristor remains relatively stable across different voltage biases. Fig. 4e and f depict the resistance value responses of HGY- and HLP-memristors at various voltage amplitudes, respectively. The resistance signal of the HGY group exhibited an initial increase followed by a decrease, showing a clear inflection point during the continuous increase of the peak voltage from 1 to 3 V. Conversely, the resistance value of the HLP group exhibited a consistent decrease with the continuous increase in peak voltage from 1 to 3 V. On the other hand, the resistance of HGY-memristor was consistently higher than that of HLP-memristor. The reason for this may be that the modelling process of HGY rats is usually accompanied by the appearance of HLP, which manifests itself in higher blood lipid levels, and the higher resistance level may be a result of the combined effect of high blood glucose and lipids, as shown in Table S2. Hence, based on these characteristics, the HGY and HLP blood groups were largely distinguished. In the future, conducting a large number of clinical tests will be necessary to establish a more comprehensive standard for HGY and HLP monitoring.

Nowadays, blood glucose in vitro detection devices have become mature, allowing people to measure their blood glucose levels anytime and anywhere [7–9,49]. However, in vitro detection of high blood lipids remains unrealized. This study proposes a promising device designed for in vitro detection of blood lipids, based on a blood memristor and a logic circuit. In Fig. 5a, the equivalent symbol of a memristor in a circuit is shown, with the thick black line segment denoting the positive direction of the device. When the current flows in the positive direction, the device behaves as LRS, and vice versa as HRS. Leveraging this property, various types of logic gate circuits, such as OR and AND gates, can be constructed based on the fabricated memristor for promising applications [50–52]. Fig. 5b illustrates the circuit diagram of the device designed in this study for in vitro detection of HGY and HLP. It's noteworthy that the inputs and outputs are voltage, with the input voltages fixed ($V_1 = 1$ V, $V_2 = 0.1$ V). A voltage sensor is employed to connect with a memristor for real-time feedback of the voltage signal output from the circuit. The circuit simulation results of the conventional OR and AND logic gates align with the truth table (Figs. S5 and S6), validating the proper functioning of the designed monitoring devices.

Fig. 5c illustrates the stability data of control, HGY, and HLP memristors within 50 cycles. The LRS and HRS of the control and HLP groups are clearly differentiated; however, the LRS and HRS of the HGY group display a staggered distribution. Our proposed HGY and HLP detection device primarily comprises a power supply, a single OR logic gate, and a voltage sensor, as depicted in Fig. 5d. Furthermore, we configured the parameters of the memristor in the constructed circuit based on the data in Fig. 5c. Considering the non-idealities and constraints of the device [53], the control, HGY, and HLP groups were randomly selected 10 times each, corresponding to 10 circuit simulations. The resultant circuit simulation data are presented as a line graph in Fig. 5e. As the number of simulations increases, the control and HLP groups exhibit stable performance, albeit with differences in voltage output signal levels. The voltage output signal is approximately 0.55 V for the HLP group and around 0.92 V for the control group. This discrepancy arises from the fact that the control-blood memristor possesses a larger HRS/LRS ratio than the HLP-memristor, leading to a higher voltage threshold in the logic circuits. Additionally, the HGY group demonstrates significant fluctuations with an increasing number of simulations, primarily due to the interleaved distribution of the LRS and HRS of the HGY-memristor, resulting in the switching of OR and AND logic gates in the logic circuit. Overall, the designed monitoring device effectively accomplishes the in vitro detection of control, HGY, and HLP. Moving forward, it will be essential to expand the sample size to enrich the device database and facilitate the establishment of more robust monitoring standards, which will be the focus of our future study.

3. Conclusions

In conclusion, unconventional material (blood) was employed as the dielectric layer in memristor and the biomemristor with an Ag/Blood/Ti/Glass structure was fabricated. Notably, this device exhibits significant RS characteristics at lower voltage biases (0 V → 1 V → −1 V → 0 V). The observed RS phenomenon is primarily attributed to a charge conduction mode driven by Ohmic conduction and ionic rearrangement. Subsequently, we extended our investigation to include memristors fabricated using blood from rats with HGY and HLP, revealing distinct electrical characteristics compared to memristors derived from healthy rat blood. Importantly, we introduce a novel device incorporating a blood memristor logic circuit, with potential applications in the in vitro detection of HGY and HLP. The device comprises a power supply, a blood memristor, and a voltage sensor. Circuit simulation results validate the effectiveness of this detection device in distinguishing normal blood, HGY blood, and HLP blood. These results make memristors compatible with logic circuits and medical in vitro monitoring, broadening the path for memristor-based biomedical applications.

4. Experiment and methods

4.1. Blood collection

Collection of fresh blood from rats. A large, healthy rat was preselected and anesthetized. Then, the hair on the neck was clipped, followed by stabbing along the jugular vein in a parallel direction using a hypodermic needle to extract an appropriate amount of fresh blood. The above blood collection process was carried out on an ultra-clean bench. The rat HGY model was established using excess high glucose chow feeding combined with STZ intraperitoneal injections (small amount and multiple times). The HLP rat model was established through continuous feeding of high-fat chow. All rats were obtained from the First Affiliated Hospital of Xi'an Jiaotong University. The final blood glucose and lipid levels in blood samples from the different rat models are presented in Table S2. All animals received humane care and the study protocolscomply with the quidelines of animal care in experiments of the First Affiliated Hospital of Xi'an Jiaotong University.

4.2. Device fabrication

In this study, the biomemristor with Ag/Blood/ITO structure (Fig. S3) was first fabricated using a typical double-ended structure. Specifically, we first dropped 100 μL of fresh blood onto a commercially available ITO substrate (2 × 2 cm, bottom electrode), and then the blood was applied to the substrate by spin-coating (500 rpm, 10 s). After the blood was naturally coagulated, metallic silver (Ag) sputtered on the blood film using a magnetron sputtering apparatus was used as the top electrode of the device. The essential sputtering parameters included a chamber pressure of 1.2 pa, a DC voltage of 70 W, 15 min and a sample tray speed of 3 rpm. Here, a typical Ag/Blood/ITO-structure memristor was fabricated. Considering the possible influence of the indium tin oxide coating on the surface of the ito substrate on the experimental results, we only replaced the substrate of the blood memristor with a glass sheet sputtered with titanium metal (Ti), while ensuring the consistency of other processes. Similarly, the sputtering process parameters for Ti mainly include a chamber pressure of 1.2 pa, a DC voltage of 70 w for 20 min, and a sample tray rotation speed of 3 rpm, whereby a typical Ag/Blood/Ti/Glass-structure memristor was fabricated. In addition, the HLP model was established based on continuous feeding of excess high-fat chow. The method of blood collection was kept consistent with that of healthy rats. In addition, we have fabricated memristors based on the blood of rats with HGY and HLP diseases, which were labeled as HGY-memristor and HLP-memristor, respectively. These devices also follow the same fabrication process as described above.

4.3. Device characterization

The electrical characteristics of the devices were tested using an electrochemical workstation equipped with a source meter (B2901B, Keysight, Beijing, China). The cross-sectional morphology of the memristor with Ag/Blood/Ti/Glass structure was observed by SEM. The chemical composition of the blood in the dielectric layer of the device was analyzed by EDS and FT-IR (Fig. S2). Finally, the construction and simulation of the blood memristor-based logic circuit was realized through the Simulink unit in MATLAB. The input and output of the circuit were voltage signals, where the input voltages were fixed at 0.1 V and 1 V respectively.

CRediT authorship contribution statement

Kaikai Gao: Writing – original draft, Methodology, Investigation, Data curation. **Bai Sun:** Writing – review & editing, Supervision, Funding acquisition. **Guangdong Zhou:** Methodology. **Zelin Cao:** Methodology. **Linbiao Xiang:** Methodology. **Jiawei Yu:** Methodology. **Ruixin Wang:** Methodology. **Yingmin Yao:** Software. **Fulai Lin:** Resources. **Zhuoqun Li:** Methodology. **Fenggang Ren:** Resources. **Yi Lv:** Software. **Qiang Lu:** Writing – review & editing, Supervision.

Declaration of competing interest

The authors declare that they have no known competing financial interests or personal relationships that could have appeared to influence the work reported in this paper.

Data availability

Data will be made available on request.

Appendix A. Supplementary data

Supplementary data to this article can be found online at https://doi.org/10.1016/j.mtbio.2024.101169.

References

[1] M. Roden, G.I. Shulman, The integrative biology of type 2 diabetes, Nature 576 (2019) 51–60, https://doi.org/10.1038/s41586-019-1797-8.
[2] B. Bozkurt, D. Aguilar, A. Deswal, S.B. Dunbar, G.S. Francis, T. Horwich, M. Jessup, M. Kosiborod, A.M. Pritchett, K. Ramasubbu, C. Rosendorff, C. Yancy, Contributory risk and management of comorbidities of hypertension, obesity, diabetes mellitus, hyperlipidemia, and metabolic syndrome in chronic heart failure: a scientific statement from the american heart association, Circulation 134 (2016) e535–e578, https://doi.org/10.1161/CIR.0000000000000450.
[3] E. Poggiogalle, H. Jamshed, C.M. Peterson, Circadian regulation of glucose, lipid, and energy metabolism in humans, Metabolism 84 (2018) 11–27, https://doi.org/10.1016/j.metabol.2017.11.017.
[4] Y.T. Liu, S.Q. Zeng, W. Ji, H. Yao, L. Lin, H.Y. Cui, H.A. Santos, G.Q. Pan, Emerging theranostic nanomaterials in diabetes and its complications, Adv. Sci. 9 (3) (2021) 2102466, https://doi.org/10.1002/advs.202102466.
[5] J. Miao, A.V. Ling, P.V. Manthena, M.E. Gearing, M.J. Graham, R.M. Crooke, K.J. Croce, R.M. Esquejo, C.B. Clish, D. Vicent, S.B. Biddinger, Flavin-containing monooxygenase 3 as a potential player in diabetes-associated atherosclerosis, Nat. Commun. 6 (2015) 6498, https://doi.org/10.1038/ncomms7498.
[6] S. Eid, K.M. Sas, S.F. Abcouwer, E.L. Feldman, T.W. Gardner, S. Pennathur, P.E. Fort, New insights into the mechanisms of diabetic complications: role of lipids and lipid metabolism, Diabetologia 62 (9) (2019) 1539–1549. https://doi.org/10.1007/s00125-019-4959-1.
[7] A.L. Galant, R.C. Kaufman, J.D. Wilson, Glucose: detection and analysis, Food Chem. 188 (2015) 149–160. https://doi.org/10.1016/j.foodchem.2015.04.071.
[8] T. Martens, R.W. Beck, R. Bailey, K.J. Ruedy, P. Calhoun, A.L. Peters, R. Pop-Busui, A. Philis-Tsimikas, S.C. Bao, G. Umpierrez, G. Davis, D. Kruger, A. Bhargava, L. Young, J.B. McGill, G. Aleppo, Q.T. Nguyen, I. Orozco, W. Biggs, K.J. Lucas, W.H. Polonsky, J.B. Buse, D. Price, R.M. Bergenstal, M.S. Group, Effect of continuous glucose monitoring on glycemic control in patients with type 2 diabetes treated with basal insulin a randomized clinical trial, JAMA 325 (22) (2021) 2262–2272. https://doi:10.1001/jama.2021.7444.
[9] Amer Diabet Assoc, 7, Diabetes technology: standards of medical care in diabetes-2021, Diabetes Care 44 (2021) S85–S99. https://doi:10.2337/dc21-S007.
[10] W. Gao, S. Emaminejad, H.Y.Y. Nyein, S. Challa, K. Chen, A. Peck, H.M. Fahad, H. Ota, H. Shiraki, D. Kiriya, D.H. Lien, G.A. Brooks, R.W. Davis, A. Javey, Fully integrated wearable sensor arrays for multiplexed in situ perspiration analysis, Nature 529 (2016) 509–514. https://doi:10.1038/nature16521.
[11] C.M. Boutry, Y. Kaizawa, B.C. Schroeder, A. Chortos, A. Legrand, Z. Wang, J. Chang, P. Fox, Z.N. Bao, A stretchable and biodegradable strain and pressure sensor for orthopaedic application, Nat. Electron. 1 (2018) 314–321. https://doi:10.1038/s41928-018-0071-7.
[12] J.W. Xu, C.C. Liang, Z.D. Gao, Y.Y. Song, Construction of nanoreactors on TiO$_2$ nanotube arrays as a POCT device for sensitive colorimetric detection, Chin. Chem. Lett. 34 (2023) 107863. https://doi:10.1016/j.cclet.2022.107863.
[13] X.M. Su, X.Y. Liu, Y.C.Z. Xie, M.Y. Chen, C. Zheng, H. Zhong, M. Li, Integrated SERS-vertical flow biosensor enabling multiplexed quantitative profiling of serological exosomal proteins in patients for accurate breast cancer subtyping, ACS Nano 17 (2023) 4077–4088. https://doi:10.1021/acsnano.3c00449.
[14] S.A. Pullano, M. Greco, M.G. Bianco, D. Foti, A. Brunetti, A.S. Fiorillo, Glucose biosensors in clinical practice: principles, limits and perspectives of currently used devices, THERANOSTICS 12 (2) (2022) 493–511. https://doi:10.7150/thno.64035.
[15] P. Li, G.H. Lee, S.Y. Kim, S.Y. Kwon, H.R. Kim, S. Park, From diagnosis to treatment: recent advances in patient-friendly biosensors and implantable devices, ACS Nano 15 (2) (2021) 1960–2004. https://doi:10.1021/acsnano.0c06688.
[16] Z.W. Zhang, P. Ma, R. Ahmed, J. Wang, D. Akin, F. Soto, B.F. Liu, P.W. Li, U. Demirci, Advanced point-of-care testing technologies for human acute respiratory virus detection, Adv. Mater. 34 (1) (2021) 2103646. https://doi:10.1002/adma.202103646.
[17] J.B. Pang, S.A. Peng, C.Y. Hou, H.B. Zhao, Y.J. Fan, C. Ye, N. Zhang, T. Wang, Y. Cao, W.J. Zhou, D. Sun, K. Wang, M.H. Rummeli, H. Liu, G. Cuniberti, Applications of graphene in five senses, nervous system, and artificial muscles, ACS Sens. 8 (2) (2023) 482–514. https://doi:10.1021/acssensors.2c02790.
[18] L.Y. Lan, J.F. Ping, J.Q. Xiong, Y.B. Ying, Sustainable natural bio-origin materials for future flexible devices, Adv. Mater. 9 (15) (2022) 2200560. https://doi:10.1002/advs.202200560.
[19] D.B. Strukov, G.S. Snider, D.R. Stewart, R.S. Williams, The missing memristor found, Nature 453 (7191) (2008) 80–83. https://doi:10.1038/nature08166.
[20] P. Yao, H.Q. Wu, B. Gao, J.S. Tang, Q.T. Zhang, W.Q. Zhang, J.J. Yang, H. Qian, Fully hardware-implemented memristor convolutional neural network, Nature 2020 577 (7792) (2020) 641–646. https://doi:10.1038/s41586-020-1942-4.
[21] M.A. Zidan, J.P. Strachan, W.D. Lu, The future of electronics based on memristive systems, Nat. Electron. 1 (1) (2018) 22–29. https://doi:10.1038/s41928-017-0006-8.
[22] F.X. Cai, J.M. Correll, S.H. Lee, Y. Lim, V. Bothra, Z.Y. Zhang, M.P. Flynn, W.D. Lu, A fully integrated reprogrammable memristor-CMOS system for efficient multiply-accumulate operations, Nat. Electron. 2 (7) (2019) 290–299. https://doi:10.1038/s41928-019-0270-x.
[23] C. Li, D. Belkin, Y.N. Li, P. Yan, M. Hu, N. Ge, H. Jiang, E. Montgomery, P. Lin, Z.R. Wang, W.H. Song, J.P. Strachan, M. Barnell, Q. Wu, R.S. Williams, J.J. Yang, Q.F. Xia, Efficient and self-adaptive in-situ learning in multilayer memristor neural networks, Nat. Commun. 9 (2018) 2385. https://doi:10.1038/s41467-018-04484-2.
[24] Z.R. Wang, C. Li, W.H. Song, M.Y. Rao, D. Belkin, Y.N. Li, P. Yan, H. Jiang, P. Lin, M. Hu, J.P. Strachan, N. Ge, M. Barnell, Q. Wu, A.G. Bartos, Q.R. Qiu, R.S. Williams, Q.F. Xia, J.J. Yang, Reinforcement learning with analogue memristor arrays, Nat. Electron. 2 (3) (2019) 115–124. https://doi:10.1038/s41928-019-0221-6.
[25] J.H. Yoon, Z.R. Wang, K.M. Kim, H.Q. Wu, V. Ravichandran, Q.F. Xia, C.S. Hwang, J.J. Yang, An artificial nociceptor based on a diffusive memristor, Nat. Commun. 9 (2018) 417. https://doi:10.1038/s41467-017-02572-3.
[26] J. Aziz, M.F. Khan, D. Neumaier, Z. Miao, E. Elahi, H. Kim, V.D. Chavan, F. Ghafoor, A.A. Ghfar, K.D. Kadam, H. Patil, Controlled charge transport in ZrO2 and its bilayer structures for low-power memory, J. Alloys Compd. 1001 (2024) 175103, https://doi.org/10.1016/j.jallcom.2024.175103.
[27] J.Q. Xu, X.N. Zhao, X.L. Zhao, Z.Q. Wang, Q.X. Tang, H.Y. Xu, Y.C. Liu, Memristors with biomaterials for biorealistic neuromorphic applications, Small Sci 2 (2022) 2200028, https://doi.org/10.1002/smsc.202270020.
[28] J. Zhang, J.M. Du, C. Yang, H.T. Liang, Z.L. Cao, X.G. Duan, W.T. Yan, Y. Zhao, B. Sun, Memristor based electronic devices towards biomedical applications, J. Mater. Chem. C 12 (2024) 50–59, https://doi.org/10.1039/D3TC03034B.
[29] X.B. Yan, X.Y. Li, Z.Y. Zhou, J.H. Zhao, H. Wang, J.J. Wang, L. Zhang, D.L. Ren, X. Zhang, J.S. Chen, C. Lu, P. Zhou, Q. Liu, Flexible transparent organic artificial synapse based on the tungsten/egg albumen/indium tin oxide/polyethylene terephthalate memristor, ACS Appl. Mater. Interfaces 11 (2019) 18654–18661, https://doi.org/10.1021/acsami.9b04443.
[30] T.R. Desai, T.D. Dongale, S.R. Patil, A.P. Tiwari, P.K. Pawar, R.K. Kamat, T.G. Kim, Synaptic learning functionalities of inverse biomemristive device based on trypsin

for artificial intelligence application, J. Mater. Res. Technol. 11 (2021) 1100–1110, https://doi.org/10.1016/j.jmrt.2021.01.108.

[31] G.D. Zhou, Z.J. Ren, B. Sun, J.G. Wu, Z. Zou, S.H. Zheng, L.D. Wang, S.K. Duan, Q. L. Song, Capacitive effect: an original of the resistive switching memory, Nano Energy 68 (2020) 104386. https://doi.org/10.1016/j.nanoen.2019.104386.

[32] T. Riaz, R. Zeeshan, F. Zarif, K. Ilyas, N. Muhammad, S.Z. Safi, A. Rahim, S.A. A. Rizvi, I.U. Rehman, FTIR analysis of natural and synthetic collagen, Appl. Spectrosc. Rev. 53 (9) (2018) 703–746. https://doi.org/10.1080/05704928.2018.1 426595.

[33] M. Khanmohammadi, A.B. Garmarudi, M. Ramin, K. Ghasemi, Diagnosis of renal failure by infrared spectrometric analysis of human serum samples and soft independent modeling of class analogy, Microchem. J. 106 (2013) 67–72. https://doi.org/10.1016/j.microc.2012.05.006.

[34] F. Yu, L.Q. Zhu, W.T. Gao, Y.M. Fu, H. Xiao, J. Tao, J.M. Zhou, Chitosan-based polysaccharide-gated flexible indium tin oxide synaptic transistor with learning abilities, ACS Appl. Mater. Interfaces 10 (19) (2018) 16881–16886. https://doi.org/10.1021/acsami.8b03274.

[35] S. Majumdar, B.B. Chen, Q.H. Qin, H.S. Majumdar, S. van Dijken, Electrode dependence of tunneling electroresistance and switching stability in organic ferroelectric P(VDF-TrFE)-based tunnel junctions, Adv. Funct. Mater. 28 (15) (2018) 1703273. https://doi.org/10.1002/adfm.201703273.

[36] F. Cao, Z.J. Hu, T.T. Yan, E. Hong, X.L. Deng, L.M. Wu, X.S. Fang, A dual-functional perovskite-based photodetector and memristor for visual memory, Adv. Mater. 35 (44) (2023) 2304550. https://doi.org/10.1002/adma.202304550.

[37] J. Kang, T. Kim, S.M. Hu, J. Kim, J.Y. Kwak, J. Park, J.K. Park, I. Kim, S. Lee, S. Kim, Y. Jeong, Cluster-type analogue memristor by engineering redox dynamics for high-performance neuromorphic computing, Nat. Commun. 13 (1) (2022) 4040. https://doi.org/10.1038/s41467-022-31804-4.

[38] X.B. Yan, Q.O.L. Zhao, A.P. Chen, J.H. Zhao, Z.Y. Zhou, J.J. Wang, H. Wang, L. Zhang, X.Y. Li, Z.A. Xiao, K.Y. Wang, C.Y. Qin, G. Wang, Y.F. Pei, H. Li, D.L. Ren, J.S. Chen, Q. Liu, Vacancy-induced synaptic behavior in 2D WS$_2$ nanosheet-based memristor for low-power neuromorphic computing, Small 15 (24) (2019) 1901423. https://doi.org/10.1002/smll.201901423.

[39] B.L. Wang, H. Luo, X.W. Wang, E.Z. Wang, Y.F. Sun, Y.C. Tsai, H. Zhu, P. Liu, K. L. Jiang, K. Liu, Bifunctional NbS$_2$-based asymmetric heterostructure for lateral and vertical electronic devices, ACS Nano 14 (1) (2020) 175–184. https://doi.org/10.1021/acsnano.9b06627.

[40] S.M. Kim, S. Kim, L. Ling, S.E. Liu, S.L. Jin, Y.M. Jung, M. Kim, H.H. Park, V. K. Sangwan, M.C. Hersam, H.S. Lee, Linear and symmetric Li-based composite memristors for efficient supervised learning, ACS Appl. Mater. Interfaces 14 (4) (2022) 5673–8681. https://doi.org/10.1021/acsami.1c24562.

[41] M. Guo, Y.L. Zhu, R.Y. Liu, K.X. Zhao, G. Dou, An associative memory circuit based on physical memristors, Neurocomputing 472 (2022) 12–23. https://doi.org/10.1016/j.neucom.2021.11.034.

[42] S. Kim, C. Du, P. Sheridan, W. Ma, S. Choi, W.D. Lu, Experimental demonstration of a second-order memristor and its ability to biorealistically implement synaptic plasticity, Nano Lett. 15 (3) (2015) 2203–2211. https://doi.org/10.1021/acs.nanolett .5b00697.

[43] B. Sun, T. Guo, G.D. Zhou, S. Ranjan, Y.X. Jiao, L. Wei, Y.N. Zhou, A.Y. Wu, Synaptic devices based neuromorphic computing applications in artificial intelligence, Mater. Today Phys. 18 (2021) 100393. https://doi.org/10.1016/j.mtph ys.2021.100393.

[44] P.X. Lei, H. Duan, L. Qin, X.H. Wei, R. Tao, Z.G. Wang, F. Guo, M.L. Song, W.J. Jie, J.H. Hao, High-performance memristor based on 2D layered BiOI nanosheet for low-power artificial optoelectronic synapses, Adv. Funct. Mater. 32 (25) (2022) 2201276. https://doi.org/10.1002/adfm.202201276.

[45] T. Guo, J.W. Ge, Y.X. Jiao, Y.C. Teng, B. Sun, W. Huang, H. Asgarimoghaddam, K. P. Musselman, Y. Fang, Y.N. Zhou, Y.A. Wu, Intelligent matter endows reconfigurable temperature and humidity sensations for in-sensor computing, Mater. Horizons 10 (3) (2023) 1030–1041. https://doi.org/10.1039/d2mh01491b.

[46] X.W. Wang, Z. Liu, T. Zhang, Flexible sensing electronics for wearable/attachable health monitoring, Small 13 (25) (2017) 1602790. https://doi.org/10.1002/smll. 201602790.

[47] T. Wilmanski, N. Rappaport, J.C. Earls, A.T. Magis, O. Manor, J. Lovejoy, G. S. Omenn, L. Hood, S.M. Gibbons, N.D. Price, Blood metabolome predicts gut microbiome α-diversity in humans, Nat. Biotechnol. 37 (10) (2019) 1217–1228. https://doi.org/10.1038/s41587-019-0233-9.

[48] F. Pan, S. Gao, C. Chen, C. Song, F. Zeng, Recent progress in resistive random access memories: materials, switching mechanisms, and performance, Mater. Sci. Eng. R Rep. 83 (2014) 1–59. https://doi.org/10.1016/j.mser.2014.06.002.

[49] V. Myndrul, E. Coy, N. Babayevska, V. Zahorodna, V. Balitskyi, I. Baginskiy, O. Gogotsi, M. Bechelany, M.T. Giardi, I. Iatsunskyi, MXene nanoflakes decorating ZnO tetrapods for enhanced performance of skin-attachable stretchable enzymatic electrochemical glucose sensor, Biosens. Bioelectron. 207 (2022) 114141. https://doi.org/10.1016/j.bios.2022.114141.

[50] B. Sun, Y. Chen, G. Zhou, Z. Cao, C. Yang, J. Du, X. Chen, J. Shao, Memristor-based artificial chips, ACS Nano 18 (2024) 14–27, https://doi.org/10.1021/ acsnano.3c07384.

[51] K.K. Gao, B. Sun, Z.L. Cao, X.G. Duan, W.T. Yan, G.Q. Tong, G.D. Zhou, X.L. Chen, J.Y. Shao, Biomaterial/organic heterojunction based memristor for logic gate circuit design, data encryption, and image reconstruction, Adv. Funct. Mater. (2024) 2401132, https://doi.org/10.1002/adfm.202401132.

[52] M. Khalid, S. Mukhtar, M. Siddique, S. Ahmed, Memristor based full adder circuit for better performance, Trans. Electr. Electron. Mater. 20 (2019) 403. https://doi.org/10.1007/s42341-019-00135-5.

[53] Z. Tang, R. Zhao, L. Luo, H. Wang, C. Lu, Constraints-aware training (CAT) to enable software-hardware co-design for memristor-based analog neuromorphic chip, HPSR (2023) 20–26. https://doi.org/10.1109/HPSR57248.2023.10148030.